Applied Surface Science 498 (2019) 143851

Contents lists available at ScienceDirect

Applied Surface Science

journal homepage: www.elsevier.com/locate/apsusc

Full length article

Large-area adlayer-free single-layer h-BN film achieved by controlling intercalation growth

Yanwei He[a,1], Hao Tian[a,1], Alireza Khanaki[a], Wenhao Shi[a], Jason Tran[b], Zhenjun Cui[a], Peng Wei[b], Jianlin Liu[a,*]

[a] Department of Electrical and Computer Engineering, University of California, Riverside, CA 92521, USA
[b] Department of Physics and Astronomy, University of California, Riverside, CA 92521, USA

ARTICLE INFO

Keywords:
Hexagonal boron nitride (h-BN)
Molecular beam epitaxy (MBE)
Intercalation
Two-dimensional (2D)
Single- and multi- layer

ABSTRACT

Controllable wafer-scale growth is one of the ultimate goals in two-dimensional (2D) h-BN synthesis, which is not fully accomplished to date. One of critical issues is the formation of three-dimensional (3D) islands (adlayers) within 2D layers, thus the films are non-uniform in thickness. In this paper, we present a study of h-BN adlayer growth and provide a strategy towards eliminating these adlayers for the precise control of the number of 2D layers. By varying the growth parameters such as substrate property, nitrogen source composition, and substrate carburization time, we found that the adlayer growth can be controlled by controlling the nucleation and intercalation processes, which is achieved by engineering the defects and impurities on substrate and the activeness of the h-BN edges. While crystallographic defects and impurities stimulate the multilayer nucleation process, activated edge tends to turn off the intercalation process by reducing the probability of precursors penetrating into the interface. We have achieved the growth of a large-area adlayer-free single-layer h-BN film.

1. Introduction

Since the isolation of single-layer graphene in 2004 [1], 2D materials have been intensively investigated, resulting in many novel devices that have unparalleled performances [2–6]. Many of these applications require precise control of film thickness. For example, single layer film may act as perfect encapsulation or insulation for other 2D materials, while multilayer film is used as excellent tunneling barrier or robust field-effect dielectric for tunneling devices and transistors, respectively. Further accurate control of the number of atomic layers in vertical heterostructures also potentially maximizes the performance of the devices based on these structures. However, while progress has been made in the scalable growth on several catalyst metal substrates [7–13], the precise control of its thickness has remained a great challenge. Non-uniform adlayers in h-BN growth are frequently observed, which compromise the uniformity and flatness of films. Thus, understanding of the formation of adlayers can provide insight into the growth of uniform 2D layers. Specifically, single-layer film can be achieved if adlayer growth is eliminated. In contrast, large multilayer film can be achieved if each layer of the adlayer seeds can grow uniformly in the lateral direction.

To date, the growth mechanism of adlayers remains elusive. One proposed mechanism suggests that sequential layers grow on top of existing layers with an assistance of defective nucleation sites [14], while others suggest that sequential layers grow underneath through intercalation [15] or precipitation [16]. Similar debate exists in graphene growth for a long time. Some propose that sequential graphene layers grown on top originate from multilayer seed [17]. For example, Kidambi et al. reported on-top growth mechanisms by using hydrogen etching [15]. On the other hand, Li et al. demonstrated that the second layer grows underneath the first layer on Cu foil by carbon isotope labeling [18]. Also in graphene/h-BN heterostructure growth, intercalation growth of graphene under h-BN cover on Ni substrate was directly observed by in situ low-energy electron microscope (LEEM) [19]. On the other hand, direct growth of graphene on exfoliated h-BN was also achieved under an extremely high growth temperature of 1850 °C [20]. Thus, whether sequential layers grow on top or from bottom depends on the growth conditions and techniques used.

2D h-BN layers are synthesized using various methods such as atomic layer deposition (ALD) [21–23], chemical vapor deposition (CVD) [10,16,24–28], and molecular beam epitaxy (MBE) [29–36]. Each one has its own merits. For example, the ALD technique can

* Corresponding author.
E-mail address: jianlin@ece.ucr.edu (J. Liu).
[1] These authors contributed equally to this work.

https://doi.org/10.1016/j.apsusc.2019.143851
Received 11 April 2019; Received in revised form 5 August 2019; Accepted 31 August 2019
Available online 02 September 2019
0169-4332/

produce h-BN films with relatively high quality at low growth temperature. Low-temperature process is important for some device applications. CVD process usually requires high temperature to decompose gaseous sources, but it is relatively simple, thus perhaps it is the most popular method. As an alternative, MBE is versatile for the synthesis of 2D h-BN due to its great controllability of growth parameters and in situ atomic-layer monitoring technique such as reflection high-energy electron diffraction (RHEED). In our recent paper regarding the MBE growth of 2D h-BN films on carburized Co and Ni substrates, we demonstrated that subsurface carbon interstitials enhance the absorption and diffusion of B and N atoms on the surface for promoting the h-BN growth [37]. Here, we focus on a study of the growth of h-BN adlayers. We used two different nitrogen sources, namely nitrogen plasma and ammonia to study the influence of hydrogen atoms; used polycrystalline Co, polycrystalline Ni, and single crystalline Ni substrates to study the influence of substrate crystallographic defects; and used different substrate carburization time to study the interstitial carbon effect. The samples were characterized by X-ray photoelectron spectroscopy (XPS), atomic force microscopy (AFM), Raman spectroscopy, scanning electron microscopy (SEM), and transmission electron microscopy (TEM). By optimizing these growth parameters, we achieved the growth of a large-area adlayer-free single-layer h-BN film, and thus this study provides a strategy towards uniform h-BN 2D film growth.

2. Methods

A Perkin-Elmer MBE system with a background pressure of $\sim 10^{-9}$ Torr was used for the sample growth. Boron was supplied by a Knudsen effusion cell filled with B_2O_3 powder (Alfa Aesar, 99.999% purity), which is heated up to around 1150 °C. Nitrogen plasma was produced by introducing nitrogen gas (Airgas, 99.9999% purity) through an electron cyclotron resonance (ECR) nitrogen plasma generator. ECR current was set at 60 mA with a power of 228 W. Ammonia (American Gas Group, 99.9995% purity) was introduced independently through another channel. Gas flow rate of each nitrogen source is limited up to 10 sccm by a mass flow controller (MFC), and total gas flow rate is limited up to 15 sccm by the turbo pump ability. Before growth, Co and Ni substrates with a size of 1 cm × 1 cm, a thickness of 0.1 mm, and a purity of 99.995% were mechanically polished, then cleaned with acetone, IPA and diluted hydrochloric acid (10%), and deionized (DI) water. All samples were grown at a substrate temperature of 900 °C. Without specific notification, the growth on Ni lasts 6 h, and on Co lasts 3 h.

SEM images were acquired using a FEI NNS450 system in secondary electron (SE) imaging mode with a beam voltage of 10 kV. Raman characterizations were performed using a HORIBA LabRam system equipped with a 60-mW, 532-nm green laser. AFM images were obtained using a Veeco D5000 AFM system. TEM images and selected area electron diffraction (SAED) patterns were acquired using a FEI Tecnai12 system. TEM sample was prepared by picking a transferred h-BN film using a 200-mesh Cu grid covered with holey carbon film with orthogonal array of 1.2-μm diameter holes. XPS characterization was conducted using a Kratos AXIS ULTRA XPS system equipped with an Al Kα monochromatic X-ray source and a 165-mm mean radius electron energy hemispherical analyzer. The fitting of XPS data was performed using CasaXPS software.

3. Results and discussion

We performed experiments based on three major growth factors, namely hydrogen, substrate type, and substrate carburization level. Fig. 1(i) and (ii) show two rows of SEM images of as grown films using different "N_2 plasma + ammonia" mixture, respectively. The numbers on the SEM images stand for the gas flow rates (sccm) of N_2 plasma and ammonia, respectively. While the samples in Fig. 1(i) were grown on polycrystalline Co, those in Fig. 1(ii) were grown on polycrystalline Ni. Thin h-BN film appears to be darker than bare metal surface due to the attenuation effect, while thick h-BN adlayers appear to be bright due to charging effect [38]. Before growth, the substrates were annealed at 900 °C in hydrogen environment for 20 min to remove native oxide layers, then carburized with 0.5-sccm C_2H_2 for 1 min to promote the adsorption and diffusion of B and N atoms [37]. Immediately after these substrate treatments, the growth for all h-BN samples took place by introducing B sources from a B_2O_3 effusion cell at 1150 °C and N mixture sources at a substrate temperature of 900 °C. After the growth, the substrate was cooled to room temperature at a rate of about 10 °C/min. Other growth details are described in the Methods section. Clear h-BN morphology transformation was demonstrated in the images from left to right on both Ni and Co substrates, as more adlayers appear with the increased amount of ammonia. However, there are fewer adlayers on Ni than on Co under the same growth conditions, therefore the h-BN morphology transformation on Ni is less drastic. Fig. 1(iii) shows SEM images of films grown on Co with different carburization time. For this batch of samples, the nitrogen source of "10 + 5" mixture was used. As shown in Fig. 1(iii), while continuous 2D h-BN films have been formed in all samples, introducing more carbon into Co results in fewer adlayers. Similar change of the adlayer density with the level of carburization is also observed for the samples grown using shorter growth duration of 1 h (Fig. S1, Supplementary Information). With the same carburization, nitrogen and boron source flux rates also have influence on the growth of adlayers. Fig. 1(iv) shows SEM images of samples grown with different B_2O_3 effusion cell temperature and the same 10-sccm ammonia. Fig. 1(v) shows SEM images of samples grown with different ammonia flux and the same B_2O_3 effusion cell temperature of 1150 °C. As can be seen, increasing the source flux rate of either boron or nitrogen results in larger coverage at the same growth duration, which indicates larger growth speed. Meanwhile, adlayers appear in all samples, and their density increases with the increase of source flux rate.

Before discussing how these three factors influence the morphology of adlayers, we briefly discuss how the adlayers may have been formed in our case, namely, whether the adlayers are formed by growing sequential layers from top of or underneath existing layers. In general, growth without metal surface catalysis requires extreme growth conditions, such as high partial pressure (e.g. ambient pressure) [39], high temperature [20,40,41], or special technique [42] to overcome the activation barrier, and the resulted films often have low coverage and uniformity [43]. On the other hand, direct growth on transition metal surface can be achieved at much lower temperature with higher coverage due to a reduced activation barrier by catalytic effect. Since the growth temperature we used is very low (900 °C), it is unlikely to trigger the growth of h-BN on top of the non-catalyzing surface. Till now, two growth mechanisms were reported for the growth-from-below scenario, namely, precipitation (or segregation) and intercalation. Precipitation growth refers to the segregation of source atoms from catalyst substrate, which requires a large solubility of precursor [44–47] and a tendency to form metastable carbide (for graphene growth) [48,49]. On the other hand, intercalation growth is caused by the diffusion of source atoms into the film/substrate interface, which is reported to be related to edge atom state [50,51] and interface binding [19]. Although B solubilities in Ni (~0.3 at.% at 1085 °C [52]) and Co (~0.3 at.% at 1110 °C [53]) are considerably large, N solubilities in these metals are reported to be extremely low (in Ni, ~0.004 at.% at 1550 °C [54]; in Co, ~0.017 at.% at 1600 °C [55]). Thus, those adlayers should be most probably formed by intercalation, instead of precipitation.

Since adlayers are formed from below, the growth of adlayers can be influenced mainly by two processes: one is the nucleation process; the other is the intercalation process. The growth of adlayers requires both a nucleation site to start the growth and a path for source supply in the interface. We first discuss how the nucleation process influences the

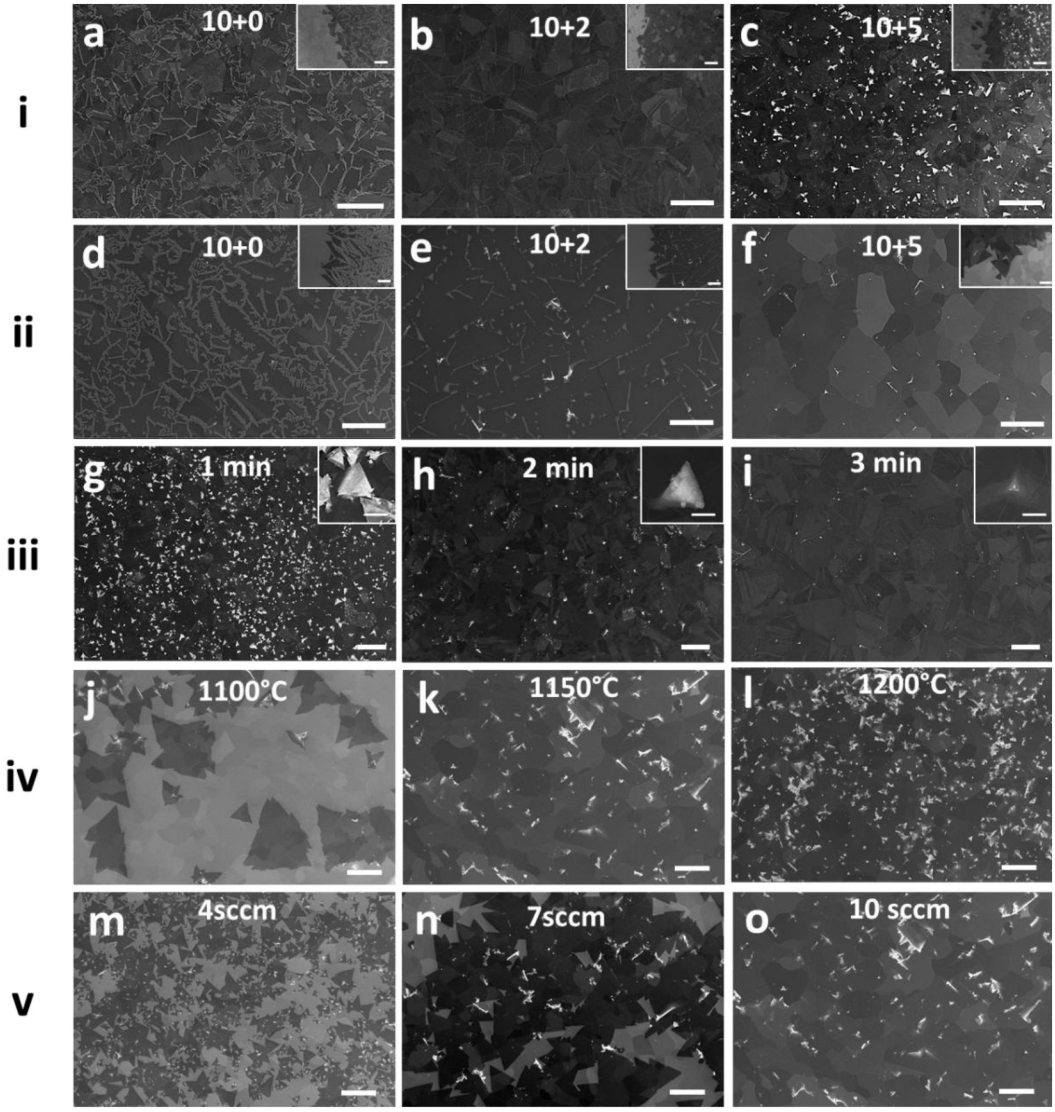

Fig. 1. SEM images for morphology evolution of h-BN at different growth condition. (i) and (ii) are samples grown with different "N_2 plasma + ammonia" mixture on Co and Ni, respectively. Insets are SEM images taken near the edge. The numbers on SEM images stand for gas flow rate (sccm). (iii) are samples grown with different carburization time on Co. Insets are close-up of adlayers. C_2H_2 gas flow rate used for carburization is 0.5 sccm, and the nitrogen mixture is 10 + 5. (iv) are samples grown with different boron source temperature on Ni with 10 sccm ammonia. (v) are samples grown with different gas flow rate of ammonia with boron cell kept 1150 °C. For samples in (i), (ii), (iv), and (v), the substrates were carburized with 0.5-sccm C_2H_2 for 1 min before growth. The scale bars for insets in (g), (h), and (i) are 50 μm, 25 μm, and 10 μm, respectively. All other scale bars are 200 μm.

adlayer growth. The detailed structures of adlayers are shown in Fig. 2. Two kinds of adlayers are observed. Fig. 2(i) shows the configuration of "prism-adlayers" with a preferential nucleation site in the center, and Fig. 2(ii) shows the configuration of "ribbon-adlayers" with preferential nucleation sites along the edges. The SEM images shown in Fig. 2a/b are taken on as grown samples, with brighter area corresponding to thicker area. Fig. 2c/d show optical microscope images of the transferred adlayers on SiO_2/Si, indicating clear thickness distribution. On "prism-adlayers", a defective nucleation site is always found in the center, as resolved by the AFM image in Fig. 2e. The line profile in Fig. 2g, which was taken across the adlayer further shows the protrusion in the center and h-BN steps around it. The narrow peaks are caused by wrinkles on h-BN. On the other hand, no discernable nucleation site is observed on "ribbon-adlayers", as shown in the AFM image of Fig. 2f. The line profile in Fig. 2h shows the decreased thickness towards the center of the flake (right hand side).

The "prism-adlayers" may originate from crystallographic defects and impurities on substrate surface, where the high surface energy is beneficial to h-BN nucleation process [14]. Multilayer seeds might form at the beginning of the growth, however, the upper layers with outer edges receive more resources than inner layers, which results in different lateral growth speeds, leading to the formation of prism-like structures. The inner layer will stop growth once it is too far away from the outmost edges, or the outmost edges merge with other flakes, which stops the intercalation process. On the other hand, the "ribbon-adlayers" are likely formed during the h-BN flake expansion. The specific reason of this kind of adlayer growth is not clear, nevertheless, it may be related to the changes of atom arrangement on substrate surface. As h-BN edges reach those regions with different atom arrangement during growth, mismatch is formed due to the loss of epitaxial relationship between h-BN film and substrate. The mismatch results in weaker binding areas where more intercalation happens [19]. B and N sources intercalate and accumulate in the confined interface, and subsequently nucleate to form atom rings and clusters, which later grow into extra layers. Similar nucleation process was reported in graphene growth [56].

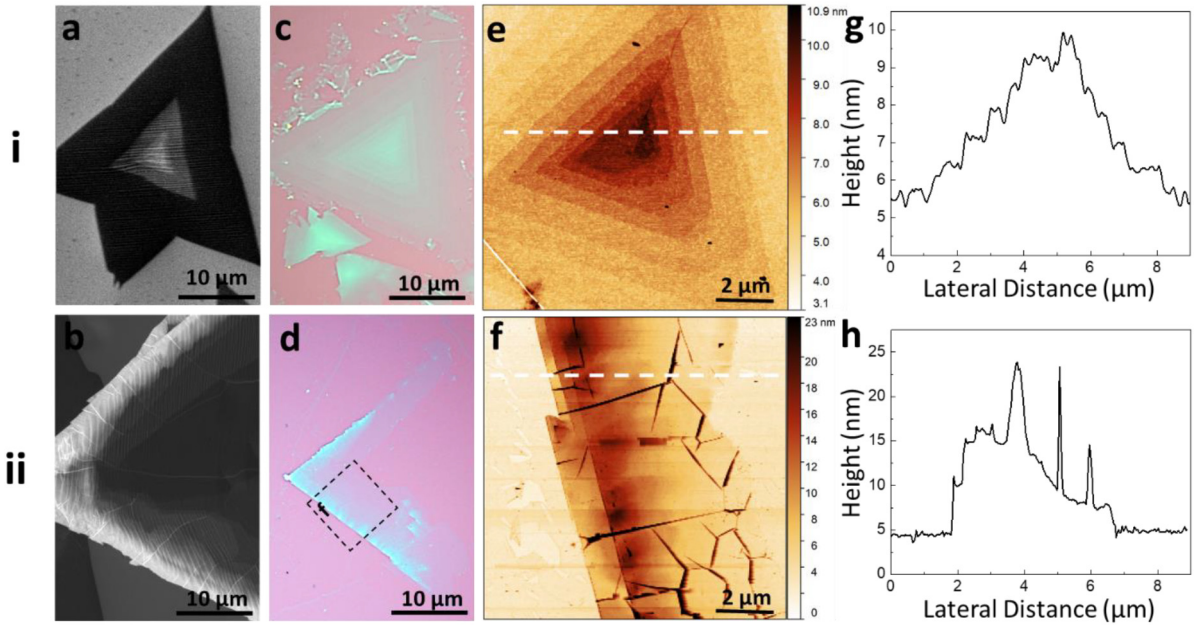

Fig. 2. Configuration of adlayers with (i) and without (ii) a nucleation site in the center. (a/b) SEM images of adlayers on as grown sample; (c/d) Optical microscope images of adlayers after transferred onto SiO_2/Si substrate; (e/f) AFM images of adlayers after transferred onto SiO_2/Si substrate; (g/h) Height profile taken along white dashed lines in e/f, respectively.

As seen from Fig. 1, even though these two kinds of adlayers coexist on every sample with adlayers, "prism-adlayers" are dominant on Co substrate, while "ribbon-adlayers" dominate on Ni surface. These adlayers can be clearly identified by using ImageJ software, and their statistical results are summarized and shown in Fig. S2 (Supplementary Information). Co and Ni are quite similar in terms of their catalytic effect [57] and B/N solubilities. However, their surface morphology is quite different after heat treatment (Fig. S3). More crystallographic defects (twin boundaries, terraces, large steps, etc.) form on Co surface than on Ni surface, which may be related to the special phase transformation of Co between HCP and FCC phases [58]. The Co surface also has worse facet uniformity, as it consists of various lattice planes. Besides FCC (111), (200), (220), there are also HCP planes. On the other hand, Ni surface is dominated by FCC (100) plane. This observation further confirms that "prism-adlayers" are related to crystallographic defects and impurities. Meanwhile, more adlayers are formed on polycrystalline Co substrate than on polycrystalline Ni substrate at the same growth condition, which may be due to the formation of more multilayer seeds on Co.

Fig. 3 shows SEM images of a sample, which was grown using the same growth conditions as the sample shown in Fig. 1k or 1o, further revealing different adlayer growth scenarios. As shown in Fig. 3a, more adlayers appear on polycrystalline region (upper right) than on single crystalline region (lower left), which illustrates the strong influence of crystallographic defects in adlayer growth. Fig. 3 b/c are adlayers grown around dents and grooves (grain boundaries) on substrate surface. Except for the adlayers directly caused by crystallographic defects, some adlayers are formed due to the intercalation near edges, such as line defects (Fig. 3d) and edges of flakes (Fig. 3e). The existence of small amount of adlayers on single crystalline region is mainly caused by impurities, as shown in Fig. 3f.

Next, we discuss how hydrogen and interstitial carbon influence the intercalation process. During the growth, N precursor is provided from two sources, namely, N_2 plasma and ammonia. While N_2 plasma is atomic source, ammonia can be regarded as molecular source. The N_2 plasma generated by ECR plasma generator consists of N_2, N_2*, N_2+, N+, N, and e-, among which only N+ (neutralizes once reaching the grounded substrate surface) and N can bond with B atom and contribute to h-BN growth. On the other hand, ammonia undergo stepwise dehydrogenation on hot metal surface, which results in NH_2, NH radicals, and N and H atoms [59]. By using different mixture of N_2 plasma and ammonia, we observed the h-BN morphology transformation from smooth sub-monolayer to non-uniform multilayer growth. As shown in Fig. 1(i) and (ii), when pure N_2 plasma was used as N source (Fig. 1a/d), as grown h-BN film is uniform without any adlayers. However, dendritic gaps (1 μm to 8 μm wide) are formed between adjacent h-BN flakes all over the surface, which do not merge even after the growth time reaches 4.5 h for the samples grown on Co (Fig. S4). Dendritic edge has been widely reported in graphene growth, which is believed to originate from the competition between adatom diffusion along island edges and adatom surface diffusion [60]. When surface diffusion is much faster, edge atoms cannot relax efficiently to find energetically more favorable locations along island edges before additional adatoms migrate by surface diffusion to join them, resulting in dendritic edges. However, our time dependent growth shows that isolated flakes are in well-defined triangle shape with straight edges (Fig. S4a), which indicates fast edge atom diffusion rate. Only when those edges of adjacent flakes approach closer, twig-like gaps are formed. The resistance to merge may be related to the bombardment effect of N_2 plasma. According to ECR plasma studies, N_2+ and N+ ions have kinetic energy ranging from 6 eV to 30 eV due to the so-called Sheath potential, which is resulted from ambipolar diffusion of ions and electrons [61]. Ions with this kinetic energy have been used for poly-Si etching, and are able to damage GaN epilayer [62]. The bombardment effect of N_2 ECR plasma on h-BN was directly proved by comparing the h-BN films grown on both front and back sides of a substrate followed by the plasma exposure as detailed in Fig. S5a-f in the Supplementary Information.

When 2-sccm ammonia was introduced in addition to 10-sccm N_2 plasma, the gaps begin to sew up (Fig. 1b, e). Since the growth pressure (2×10^{-4} Torr) did not change much, the alleviation of the plasma's bombardment effect due to mean free path change can be ignored. Instead, the "sewing effect" may be caused by hydrogen. Hydrogen atoms are known to have strong influence in graphene growth. For example, the graphene crystal patterns can be tailored by adjusting CH_4/H_2 ratio [60]; the formation of single and bilayer graphene is closely related to the presence of hydrogen [51]; super large single-crystalline graphene domain can be achieved by removing hydrogen

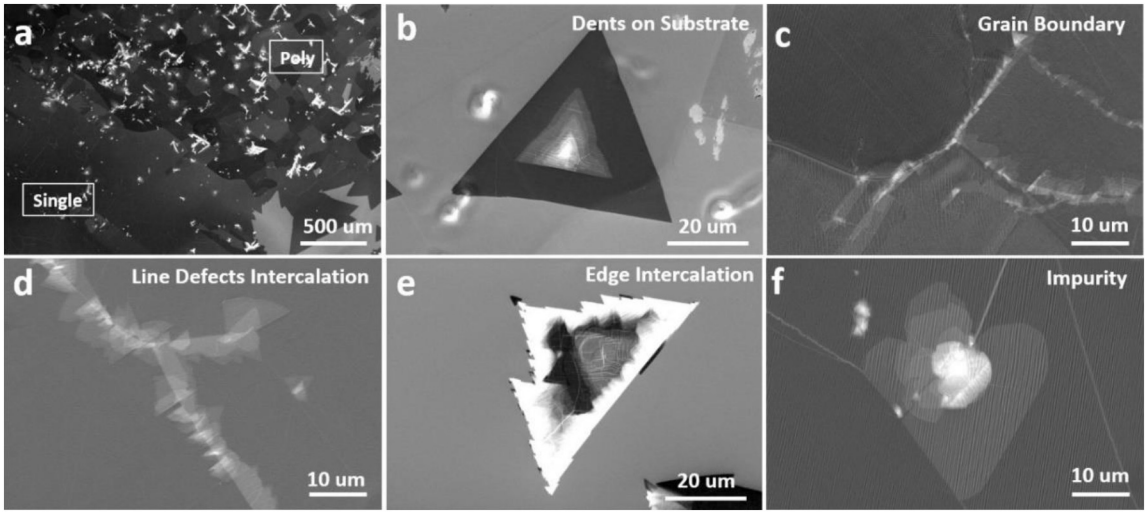

Fig. 3. SEM images of h-BN adlayers. (a) h-BN grown on Ni with polycrystalline region (upper right) and single crystalline region (lower left); (b) close-up of adlayer grown around dents on substrate surface; (c) close-up of adlayer grown along substrate grain boundary; (d) close-up of adlayer grown along h-BN line defects; (e) close-up of adlayer grown near h-BN flake edges; (e) close-up of h-BN adlayer grown around impurity.

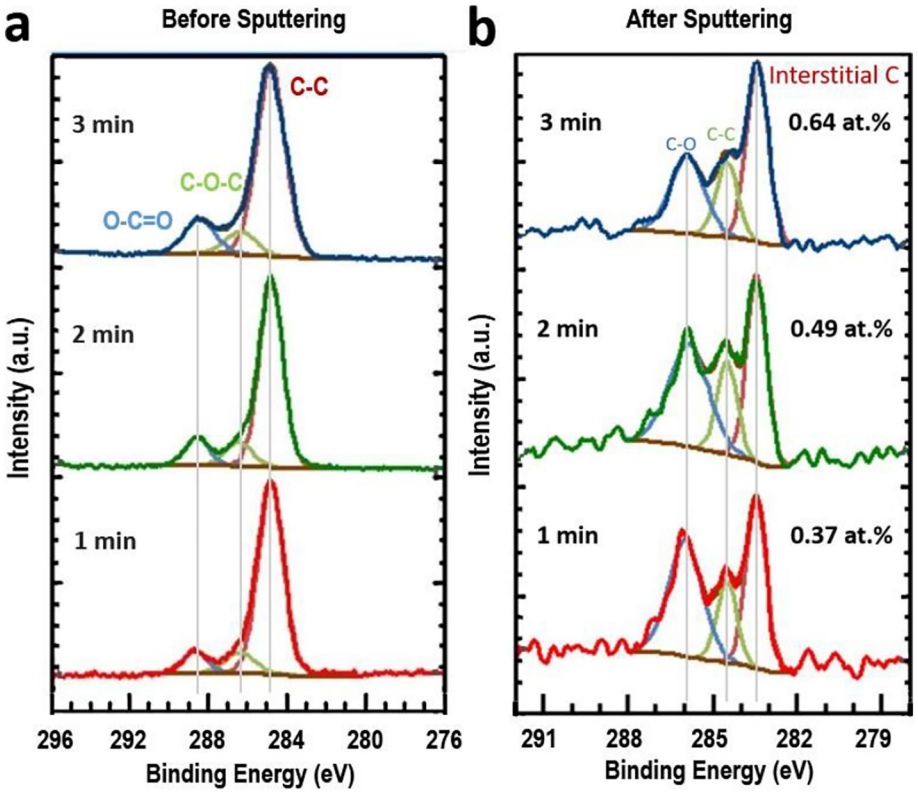

Fig. 4. XPS characterization of C_1s on samples with 1-min, 2-min, and 3-min carburization. (a) Before sputtering; (b) and after sputtering. As the carburization time increases, the subsurface carbon concentration increases.

atoms on growing edges [63]. Similar to graphene growth, hydrogen atom can also terminate h-BN edge [64,65]. The presence of hydrogen on h-BN edges can be inferred from the irregular shape of h-BN domains formed when using pure ammonia as N precursor (Fig. S4d). Hydrogen termination results in lower edge atom diffusion rate, thus edge atoms cannot relax sufficiently to find energetically more favorable locations along island edges before additional B/N atoms migrate by surface diffusion to join them. In the absence of such relaxation, irregular edges are formed [66,67]. The presence of hydrogen atoms on growing edges could have alleviated the plasma's bombardment effect, so as to make the edges easier to merge. On the other hand, the presence of hydrogen on growing edges may also be responsible for the lower lateral growth rate when using ammonia, as shown in the time-dependent growth results in Fig. S4. For the same growth time, using ammonia results in lower coverage than using N_2 plasma. Additional activation energies are needed to release hydrogen species from hydrogen terminated edge atoms and/or hydrogen-contained incoming precursors to form h-BN [63], resulting in lower growth rate.

Adlayers were formed when more ammonia was introduced (Fig. 1c/1f). As discussed above, these adlayers should be formed from below by intercalation. In graphene growth, people had reported that hydrogen atoms terminating the growing edges could result in the

intercalation growth of adlayers [50,51]. Here we propose a similar intercalation model, in which the density of B/N atoms in the interface (n_{in}) is proportional to the penetration probability j_{pene} (possibility of atoms penetrate through the edge) and the density of B/N atoms outside the edge (n_{out}). j_{pene} is a factor related to the activeness of h-BN edges, which is determined by the activation energy barrier for h-BN growth. The more active the edges are, the more likely that upcoming atoms get caught and contribute to the lateral growth, thus the less likely these atoms penetrate into the interface. n_{out} is related to source flux rate and adsorption coefficient on catalyst substrate. Larger source flux rate and adsorption coefficient would result in larger n_{out}. By passivating the edges with hydrogen, we actually increase the j_{pene}, thus more B/N atoms end up in the interface, and in turn, adlayers grow. In a hydrogen-free environment (N_2 plasma as N source), the growing edges with unpaired dangling bonds are very active and readily catch upcoming B and N atoms, thus the j_{pene} is small, leading to no adlayer growth. It is worth noting that potential use of the mixture of hydrogen and nitrogen gas as N source cannot replicate the role of ammonia because pure hydrogen gas strongly etches h-BN (Fig. S5 g/h).

Interstitial carbon embedded in the substrate affects the adlayer growth as well. The amount of interstitial carbon was controlled by the introduction time of C_2H_2 treatment of hot substrates prior to h-BN growth, and longer carburization time led to higher density of interstitial carbon in the substrate, as revealed by XPS studies. Fig. 4 shows XPS spectra of C_1s on samples with different carburization time as shown in Fig. 1(iii). As-measured XPS data was first deconvoluted, and fitted with Shirley background and GL(30) line shape. The spectrum was then calibrated by shifting C—C main peak to 284.8 eV. As shown in Fig. 4a, the C_1s signal was dominated by adventitious carbon before sputtering, with C—C/C—H peak at 284.8 eV, C—O—H/C—O—C at 286.3 eV, and O—C═O at 288.5 eV, respectively. Even with different carburization time, no discernable differences were observed before sputtering. Fig. 4b shows the C_1s peak after 60-s Ar^+ ion sputtering. From bottom to up, these are the profiles for 1-min, 2-min, and 3-min carburized samples, respectively. After sputtering, the dissolved interstitial carbon peak at 283.6 eV is resolved [68,69]. The other two small peaks at 284.8 eV and 286.3 eV are assigned to residual adventitious C—C/C—H and C—O—H/C—O—C carbon, respectively. Precipitated carbon onto grain boundaries may also contribute to the peak at 284.8 eV. No sp^2 C—C bond and Ni—C bond signals are detectable within the limit of the XPS system, suggesting no graphitic or graphene structures have been formed. Based on the depth resolved XPS data, we calculated the interstitial carbon concentration. It was found that the atomic percentage for 1-min, 2-min, and 3-min carburization is 0.37 at.%, 0.49 at.%, and 0.64 at.%, respectively. However, since the depth resolved XPS data were obtained at room temperature, the real carbon concentration at the growth temperature may be different. According to the first-principles calculation, the subsurface carbon concentration in Ni can be as high as 50 at.% before carbon atoms diffuse deep into the bulk [70], thus the carbon concentration at subsurface during growth should be proportional to carburization time.

As shown in Fig. 1 (iii), increasing the carburization time suppresses the growth of adlayers. Our previous work indicates that interstitial carbon atoms at the subsurface octahedral sites can enhance the absorption of B and N atoms on Co and Ni substrates and increase the h-BN growth speed [37]. The increased growth speed can be caused by increased source supply (n_{out}), since the absorption of B and N atoms on the surface is enhanced. It may also be caused by improved catalytic activities of the transition metals under the interstitial carbon incorporation, which results in smaller activation energy barrier for the nucleation and growth of h-BN. In other words, h-BN edges are more active in catching upcoming B and N atoms and the growth becomes faster. To elucidate how interstitial carbon exactly works, we compare it to the source flux dependent growth (Fig. 1(iv) and 1(v)), where only n_{out} is changed. As stated earlier, the increase of source flux results in the increase of growth rate. However, the amount of adlayers is also increased. This can be understood based on the intercalation model as discussed above. Since j_{pene} remains unchanged, the increase in n_{out} results in more B and N atoms in the interface, thus more growth of adlayers. On the other hand, the increase of the amount of interstitial carbon also results in larger growth speed, however, the amount of adlayers decreases (Fig. S1). This suggests that interstitial carbon does not increase h-BN growth rate simply by increasing the absorption of B/N on the surface (increase of n_{out}). It improves the catalytic effect of the substrate as well. With improved catalytic effect, not only adsorption and diffusion of B and N atoms enhance [37], but also the h-BN edges are much more ready to catch upcoming B/N atoms, therefore j_{pene} decreases, and fewer B/N atoms end up in the interface.

So far, we have discussed the factors influencing the growth of h-BN adlayer, including substrate crystallographic defects, hydrogen, and interstitial carbon. While substrate crystallographic defects have strong influence on the nucleation process, hydrogen and interstitial carbon can control the growth of adlayers by engineering the activeness of h-BN edges. Activated edges diminish intercalation growth by decreasing the penetration probability of B/N atoms, while passivated edges promote intercalation growth by increasing the penetration probability of B/N atoms. Considering all these factors, we made an attempt to achieve precise control of the number of layers. First, uniform single-layer film can be obtained by eliminating intercalation growth. To achieve this, single crystalline Ni substrate was chosen in order to diminish the formation of multilayer seeds. A mixture of 10-sccm N_2 plasma and 2-sccm ammonia was used as nitrogen source, in which the 2-sccm ammonia help alleviate plasma bombardment effect and sew the gaps between flakes. 4-min C_2H_2 carburization was used to compensate the effect from the presence of H and keep the h-BN edge active to B and N. The temperature of B_2O_3 effusion cell and substrate were kept at 1150 °C and 900 °C, respectively. The growth time was 6 h. Fig. 5a shows an SEM image of single-layer film taken at the center of as grown sample, with the inset showing the film edge area. No large adlayers were observed over the 1 cm^2 surface. Corresponding RHEED images are shown in Fig. S6, revealing the characteristic patterns of both the substrate and h-BN film. Fig. 5b shows an optical microscopy image of the transferred h-BN film on SiO_2/Si substrate. The film was transferred by modified RCA process [71], followed by an annealing at 400 °C in oxygen environment for 3 h to remove water and PMMA residue [72,73]. The transferred film shows uniform contrast in large area despite of some small contaminations (black and yellow dots), indicating high film quality. The thickness of the single-layer h-BN film was confirmed by TEM as shown in Fig. 5c. Inserted SAED pattern shows bright spots in hexagonal arrangement, indicating the hexagonal arrangement of B and N atoms. The rings in SAED pattern are formed due to the diffraction of electrons by amorphous holy carbon thin film on TEM grids. The AFM image in Fig. 5d was taken on transferred film shown in Fig. 5b. Larger thickness (0.7 nm) compared to theoretical value (0.33 nm) of single-layer film may be caused by different atomic forces between tip/h-BN and tip/SiO_2, weak binding between h-BN film and SiO_2/Si substrate, as well as water and gases intercalated in the interface [14]. Raman mapping was performed on the transferred sample, and the result is shown in Fig. 5e. The green contrast is corresponding to E_{2g} peak of h-BN. The slight nonuniformity in Raman intensity may be caused by the corrugation of h-BN film formed during transfer process. Fig. 5f shows Raman spectra extracted from nine different spots of Raman map, and all the peaks are located around 1369.5 cm^{-1}, which implies single-layer h-BN [74]. Fig. 5 g/h show XPS spectra of B_1s and N_1s signals of as grown single layer h-BN film, respectively. As-measured XPS data was first deconvoluted, and fitted with Shirley background and GL(0) line shape. These spectra were then calibrated by shifting C—C main peak to 284.8 eV. The main peaks of B and N are measured to be 190.1 eV and 397.6 eV, respectively, an indication of sp^2 bonds, which is consistent with other reports [15,16]. The smaller peak next to the main peak at higher position, 190.7 (398.2) eV, is assigned to cubic-like sp^3 bond [75,76]. The neglectable

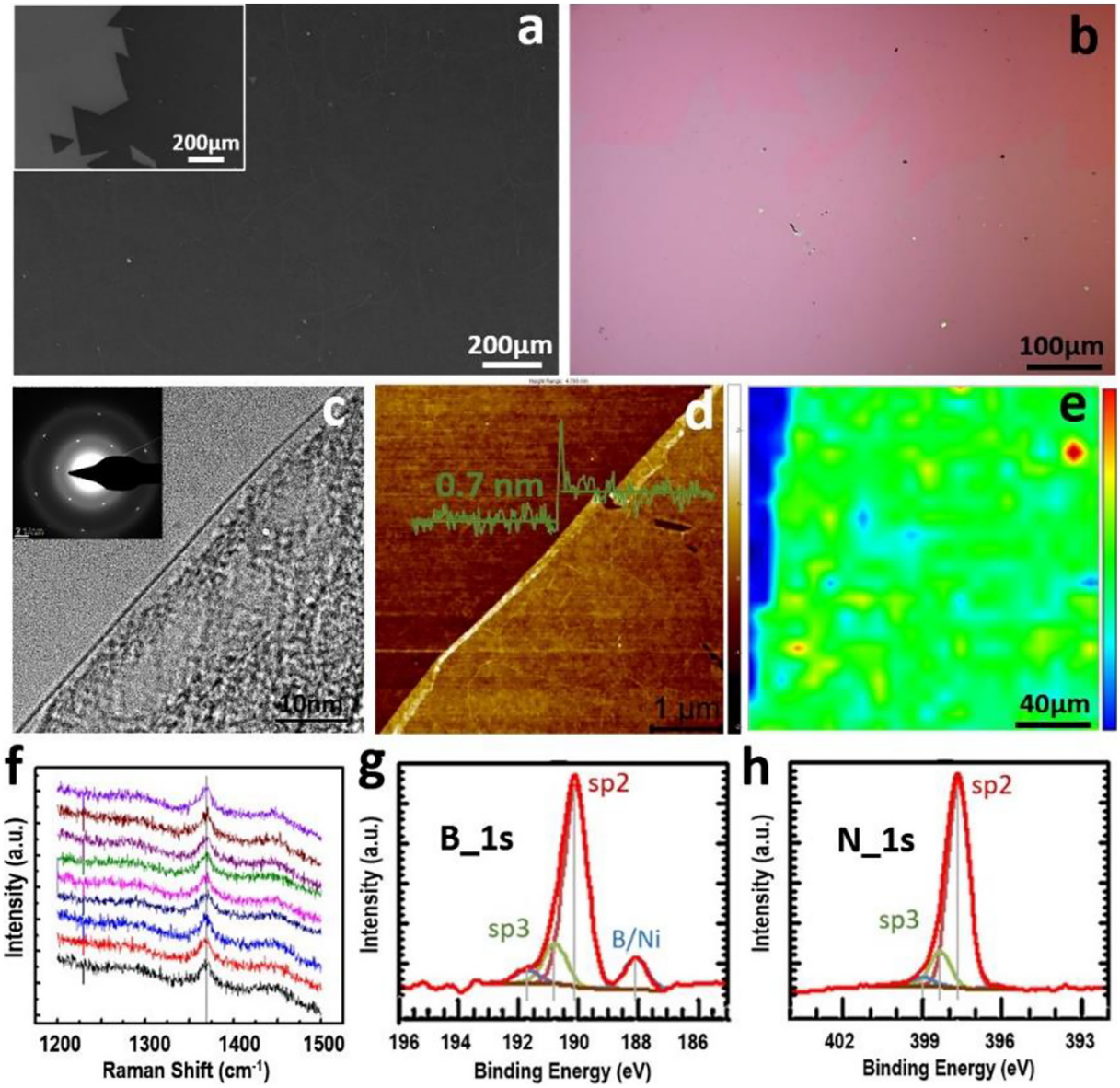

Fig. 5. Characterization of single-layer h-BN film grown on Ni. (a) SEM image of as grown sample, with the inset showing edge area of film; (b) Optical microscope image of the sample after transferred onto SiO_2/Si substrate; (c) TEM image of the sample after transferred onto TEM grid, with inset showing the SAED pattern; (c) AFM image taken on the transferred sample; (d) Raman mapping of h-BN characteristic peak on the transferred sample; (f) 9 random Raman spectra extracted from (e); (g) XPS spectrum of B_1s; (h) XPS spectrum of N_1s.

small peak at the highest position, 191.6 (399.5) eV, is assigned to oxygen related defects [77]. The boron to nitrogen ratio calculated based on XPS data is around 0.96. SEM images of growth time dependent single-layer films are shown in Fig. S7. As the growth time increases, the coverage of the h-BN single-layer film increases.

The obstacle towards large-area bilayer and multilayer growth is the differentiated growth speeds between inner and outer layers, which is caused by insufficient source supply in the interface. In other words, the h-BN growth speed lies in a source limited region. On the other hand, if sufficient B and N atoms are supplied, h-BN growth may be transitioned into a self-limited region, where the growth speed is not limited by source supply, instead, it is limited by the bond formation rate. Then the growth speed of inner edge may have a chance to catch up outer edge so that large-area bilayer or multilayer films can be achieved. Towards this end, we grew a sample with an attempt of increasing B supply. Prior to introduction of both N and B sources, we deposited B only for 30 mins with B_2O_3 cell kept at 1175 °C. The pre-deposition of B allows the saturation of B in the substrate prior to growth; it also leads to the existence of abundant B atoms on the surface, in particular around surface defects or other imperfect or irregular sites. Once N atoms are introduced, the multilayer seed nucleation may have higher chances to happen. In other words, if the growth started without B pre-deposition, portion of B atoms would diffuse into the substrate at the early growth stage due to its solubility, then less B atoms would meet N atoms to nucleate and grow into multilayer seeds at the growth stage. The result of comparing h-BN growth with and without pre-deposition of B is shown in Fig. S8. With pre-deposition, the adlayer size is significantly increased, and the second layer can reach up to 250 μm. However, improved strategy to provide sufficient B and N sources to the interface between the outmost layer and the substrate is needed to achieve wafer-scale uniform multilayer growth, which is in progress.

4. Conclusion

We have carried out a study of intercalation growth of h-BN adlayers. By comparing the growth on different catalyst substrates, we

showed that crystallographic defects on catalyst substrates play an important role in adlayer nucleation process. By using N plasma, ammonia, and their mixtures as nitrogen sources, we found that hydrogen played multiple roles in h-BN growth. On one hand, hydrogen terminating growing edges can provide protection against plasma's bombardment effect, making 2D h-BN flakes easier to merge. On the other hand, it passivates h-BN edges, which results in slower lateral growth rate and more intercalation growth of 3D adlayers. We also further revealed an important role played by interstitial carbon in the transition metal substrates, which enhances the substrate catalytic effect. The enhanced catalytic effect not only promotes the adsorption of B and N atoms, but also makes h-BN edges active in catching upcoming B and N atoms, which results in larger growth speed and less intercalation growth of adlayers. By controlling the mixture of atomic N and molecular N sources, we achieved large-area growth of adlayer-free single-layer h-BN film on a carburized single-crystalline Ni substrate. Our research work helps reveal the h-BN adlayer growth mechanism and provides insight towards controllable growth of wafer-scale h-BN 2D films with uniform thickness.

Acknowledgments

We acknowledge the support by FAME, one of six centers of STARnet, a Semiconductor Research Corporation program supported by MACRO and DARPA. This work was also in part supported by SHINES, an Energy Frontier Research Center funded by the U.S. Department of Energy, Office of Science, Basic Energy Sciences under Award #SC0012670.

Appendix A. Supplementary data

Supplementary data to this article can be found online at https://doi.org/10.1016/j.apsusc.2019.143851.

References

[1] K.S. Novoselov, A.K. Geim, S.V. Morozov, D. Jiang, Y. Zhang, S.V. Dubonos, I.V. Grigorieva, A.A. Firsov, Electric field effect in atomically thin carbon films, Science 306 (2004) 666–669, https://doi.org/10.1126/science.1102896.

[2] L. Britnell, R. Gorbachev, R. Jalil, B. Belle, F. Schedin, A. Mishchenko, T. Georgiou, M. Katsnelson, L. Eaves, S. Morozov, Field-effect tunneling transistor based on vertical graphene heterostructures, Science 335 (2012) 947–950, https://doi.org/10.1126/science.1218461.

[3] Q. Bao, K.P. Loh, Graphene photonics, plasmonics, and broadband optoelectronic devices, ACS Nano 6 (2012) 3677–3694, https://doi.org/10.1021/nn300989g.

[4] R. Cheng, D. Li, H. Zhou, C. Wang, A. Yin, S. Jiang, Y. Liu, Y. Chen, Y. Huang, X. Duan, Electroluminescence and photocurrent generation from atomically sharp WSe2/MoS2 heterojunction p–n diodes, Nano Lett. 14 (2014) 5590–5597, https://doi.org/10.1021/nl502075n.

[5] F. Withers, O. Del Pozo-Zamudio, A. Mishchenko, A. Rooney, A. Gholinia, K. Watanabe, T. Taniguchi, S. Haigh, A. Geim, A. Tartakovskii, Light-emitting diodes by band-structure engineering in van der Waals heterostructures, Nat. Mater. 14 (2015) 301, https://doi.org/10.1038/NMAT4205.

[6] A. Maity, T. Doan, J. Li, J. Lin, H. Jiang, Realization of highly efficient hexagonal boron nitride neutron detectors, Appl. Phys. Lett. 109 (2016) 072101, , https://doi.org/10.1063/1.4960522.

[7] F. Hui, M.A. Villena, W. Fang, A.-Y. Lu, J. Kong, Y. Shi, X. Jing, K. Zhu, M. Lanza, Synthesis of large-area multilayer hexagonal boron nitride sheets on iron substrates and its use in resistive switching devices, 2D Materials 5 (2018) 031011, , https://doi.org/10.1021/nl203249a.

[8] S. Caneva, R.S. Weatherup, B.C. Bayer, B. Brennan, S.J. Spencer, K. Mingard, A. Cabrero-Vilatela, C. Baehtz, A.J. Pollard, S. Hofmann, Nucleation control for large, single crystalline domains of monolayer hexagonal boron nitride via Si-doped Fe catalysts, Nano Lett. 15 (2015) 1867–1875, https://doi.org/10.1021/nl5046632.

[9] G. Kim, A.-R. Jang, H.Y. Jeong, Z. Lee, D.J. Kang, H.S. Shin, Growth of high-crystalline, single-layer hexagonal boron nitride on recyclable platinum foil, Nano Lett. 13 (2013) 1834–1839, https://doi.org/10.1021/nl400559s.

[10] K.K. Kim, A. Hsu, X. Jia, S.M. Kim, Y. Shi, M. Hofmann, D. Nezich, J.F. Rodriguez-Nieva, M. Dresselhaus, T. Palacios, Synthesis of monolayer hexagonal boron nitride on cu foil using chemical vapor deposition, Nano Lett. 12 (2011) 161–166, https://doi.org/10.1021/nl203249a.

[11] J. Meng, X. Zhang, Y. Wang, Z. Yin, H. Liu, J. Xia, H. Wang, J. You, P. Jin, D. Wang, Aligned growth of millimeter-size hexagonal boron nitride single-crystal domains on epitaxial nickel thin film, Small 13 (2017) 1604179, , https://doi.org/10.1002/smll.201604179.

[12] H. Ying, X. Li, D. Li, M. Huang, W. Wan, Q. Yao, X. Chen, Z. Wang, Y. Wu, L. Wang, Ni foam assisted synthesis of high quality hexagonal boron nitride with large domain size and controllable thickness, 2D Materials 5 (2018) 025020, , https://doi.org/10.1088/2053-1583/aab407.

[13] M. Petrović, U. Hagemann, M. Horn-von Hoegen, F.-J.M. zu Heringdorf, Microanalysis of single-layer hexagonal boron nitride islands on Ir (111), Appl. Surf. Sci. 420 (2017) 504–510, https://doi.org/10.1016/j.apsusc.2017.05.155.

[14] M.H. Khan, Z. Huang, F. Xiao, G. Casillas, Z. Chen, P.J. Molino, H.K. Liu, Synthesis of large and few atomic layers of hexagonal boron nitride on melted copper, Sci. Rep. 5 (2015) 7743, https://doi.org/10.1038/srep07743.

[15] P.R. Kidambi, R. Blume, J. Kling, J.B. Wagner, C. Baehtz, R.S. Weatherup, R. Schloegl, B.C. Bayer, S. Hofmann, In situ observations during chemical vapor deposition of hexagonal boron nitride on polycrystalline copper, Chem. Mater. 26 (2014) 6380–6392, https://doi.org/10.1021/cm502603n.

[16] S. Caneva, R.S. Weatherup, B.C. Bayer, R. Blume, A. Cabrero-Vilatela, P. Braeuninger-Weimer, M.-B. Martin, R. Wang, C. Baehtz, R. Schloegl, Controlling catalyst bulk reservoir effects for monolayer hexagonal boron nitride CVD, Nano Lett. 16 (2016) 1250–1261, https://doi.org/10.1021/acs.nanolett.5b04586.

[17] A.W. Robertson, J.H. Warner, Hexagonal single crystal domains of few-layer graphene on copper foils, Nano Lett. 11 (2011) 1182–1189, https://doi.org/10.1021/nl104142k.

[18] Q. Li, H. Chou, J.-H. Zhong, J.-Y. Liu, A. Dolocan, J. Zhang, Y. Zhou, R.S. Ruoff, S. Chen, W. Cai, Growth of adlayer graphene on Cu studied by carbon isotope labeling, Nano Lett. 13 (2013) 486–490, https://doi.org/10.1021/nl303879k.

[19] Y. Yang, Q. Fu, H. Li, M. Wei, J. Xiao, W. Wei, X. Bao, Creating a nanospace under an h-BN cover for Adlayer growth on nickel (111), ACS Nano 9 (2015) 11589–11598, https://doi.org/10.1021/acsnano.5b05509.

[20] A. Summerfield, A. Davies, T.S. Cheng, V.V. Korolkov, Y. Cho, C.J. Mellor, C.T. Foxon, A.N. Khlobystov, K. Watanabe, T. Taniguchi, Strain-engineered graphene grown on hexagonal boron nitride by molecular beam epitaxy, Sci. Rep. 6 (2016) 22440, , https://doi.org/10.1038/srep22440.

[21] J. Ferguson, A. Weimer, S. George, Atomic layer deposition of boron nitride using sequential exposures of BCl3 and NH3, Thin Solid Films 413 (2002) 16–25, https://doi.org/10.1016/S0040-6090(02)00431-5.

[22] M.S. Driver, J.D. Beatty, O. Olanipekun, K. Reid, A. Rath, P.M. Voyles, J.A. Kelber, Atomic layer epitaxy of h-BN (0001) multilayers on Co (0001) and molecular beam epitaxy growth of graphene on h-BN (0001)/Co (0001), Langmuir 32 (2016) 2601–2607, https://doi.org/10.1021/acs.langmuir.5b03653.

[23] J. Jones, B. Beauclair, O. Olanipekun, S. Lightbourne, M. Zhang, B. Pollok, A. Pilli, J. Kelber, Atomic layer deposition of h-BN (0001) on RuO2 (110)/Ru (0001), J. Vac. Sci. Technol. A 35 (2017) 01B139, , https://doi.org/10.1116/1.4972784.

[24] Y. Shi, C. Hamsen, X. Jia, K.K. Kim, A. Reina, M. Hofmann, A.L. Hsu, K. Zhang, H. Li, Z.-Y. Juang, Synthesis of few-layer hexagonal boron nitride thin film by chemical vapor deposition, Nano Lett. 10 (2010) 4134–4139, https://doi.org/10.1021/nl1023707.

[25] L. Song, L. Ci, H. Lu, P.B. Sorokin, C. Jin, J. Ni, A.G. Kvashnin, D.G. Kvashnin, J. Lou, B.I. Yakobson, Large scale growth and characterization of atomic hexagonal boron nitride layers, Nano Lett. 10 (2010) 3209–3215, https://doi.org/10.1021/nl1022139.

[26] A. Ismach, H. Chou, P. Mende, A. Dolocan, R. Addou, S. Aloni, R. Wallace, R. Feenstra, R.S. Ruoff, L. Colombo, Carbon-assisted chemical vapor deposition of hexagonal boron nitride, 2D Materials 4 (2017) 025117, , https://doi.org/10.1088/2053-1583/aa74a5.

[27] M. Petrović, M. Horn-von Hoegen, F.-J.M. zu Heringdorf, Lateral heterostructures of hexagonal boron nitride and graphene: BCN alloy formation and microstructuring mechanism, Appl. Surf. Sci. 455 (2018) 1086–1094, https://doi.org/10.1016/j.apsusc.2018.06.057.

[28] Y. Song, C. Zhang, B. Li, D. Jiang, G. Ding, H. Wang, X. Xie, Triggering the atomic layers control of hexagonal boron nitride films, Appl. Surf. Sci. 313 (2014) 647–653, https://doi.org/10.1016/j.apsusc.2014.06.040.

[29] S. Nakhaie, J. Wofford, T. Schumann, U. Jahn, M. Ramsteiner, M. Hanke, J. Lopes, H. Riechert, Synthesis of atomically thin hexagonal boron nitride films on nickel foils by molecular beam epitaxy, Appl. Phys. Lett. 106 (2015) 213108, , https://doi.org/10.1063/1.4921921.

[30] C. Tsai, Y. Kobayashi, T. Akasaka, M. Kasu, Molecular beam epitaxial growth of hexagonal boron nitride on Ni (1 1 1) substrate, J. Cryst. Growth 311 (2009) 3054–3057, https://doi.org/10.1016/j.jcrysgro.2009.01.077.

[31] Z. Zuo, Z. Xu, R. Zheng, A. Khanaki, J.-G. Zheng, J. Liu, In-situ epitaxial growth of graphene/h-BN van der Waals heterostructures by molecular beam epitaxy, Sci. Rep. 5 (2015) 14760, , https://doi.org/10.1038/srep14760.

[32] T. Vuong, G. Cassabois, P. Valvin, E. Rousseau, A. Summerfield, C. Mellor, Y. Cho, T. Cheng, J.D. Albar, L. Eaves, Deep ultraviolet emission in hexagonal boron nitride grown by high-temperature molecular beam epitaxy, 2D Materials 4 (2017) 021023, , https://doi.org/10.1088/2053-1583/aa604a.

[33] M. Heilmann, M. Bashouti, H. Riechert, J. Lopes, Defect mediated van der Waals epitaxy of hexagonal boron nitride on graphene, 2D Materials 5 (2018) 025004, , https://doi.org/10.1088/2053-1583/aaa4cb.

[34] A. Khanaki, H. Tian, Z. Xu, R. Zheng, Y. He, Z. Cui, J. Yang, J. Liu, Effect of high carbon incorporation in Co substrates on the epitaxy of hexagonal boron nitride/graphene heterostructures, Nanotechnology 29 (2017) 035602, , https://doi.org/10.1088/1361-6528/aa9c58.

[35] A. Summerfield, A. Kozikov, T.S. Cheng, A. Davies, Y.-J. Cho, A.N. Khlobystov, C.J. Mellor, C.T. Foxon, K. Watanabe, T. Taniguchi, Moiré-modulated conductance of hexagonal boron nitride tunnel barriers, Nano Lett. 18 (2018) 4241–4246, https://doi.org/10.1021/acs.nanolett.8b01223.

[36] Y.-J. Cho, A. Summerfield, A. Davies, T.S. Cheng, E.F. Smith, C.J. Mellor, A.N. Khlobystov, C.T. Foxon, L. Eaves, P.H. Beton, Hexagonal boron nitride tunnel barriers grown on graphite by high temperature molecular beam epitaxy, Sci. Rep. 6 (2016) 34474, , https://doi.org/10.1038/srep34474.
[37] H. Tian, A. Khanaki, P. Das, R. Zheng, Z. Cui, Y. He, W. Shi, Z. Xu, R. Lake, J. Liu, Role of carbon interstitials in transition metal substrates on controllable synthesis of high-quality large-area two-dimensional hexagonal boron nitride layers, Nano Lett. 18 (2018) 3352–3361, https://doi.org/10.1021/acs.nanolett.7b05179.
[38] P. Sutter, E. Sutter, Thickness determination of few-layer hexagonal boron nitride films by scanning electron microscopy and auger electron spectroscopy, APL Materials 2 (2014) 092502, , https://doi.org/10.1088/2053-1583/aad5aa.
[39] L. Tai, D. Zhu, X. Liu, T. Yang, L. Wang, R. Wang, S. Jiang, Z. Chen, Z. Xu, X. Li, Direct growth of graphene on silicon by metal-free chemical vapor deposition, Nano-Micro Letters 10 (2018) 20, https://doi.org/10.1007/s40820-017-0173-1.
[40] D. Chugh, J. Wong-Leung, L. Li, M. Lysevych, H. Tan, C. Jagadish, Flow modulation epitaxy of hexagonal boron nitride, 2D Materials 5 (2018) 045018, , https://doi.org/10.1088/2053-1583/aad5aa.
[41] S. Entani, M. Takizawa, S. Li, H. Naramoto, S. Sakai, Growth of graphene on SiO2 with hexagonal boron nitride buffer layer, Appl. Surf. Sci. 475 (2019) 6–11, https://doi.org/10.1016/j.apsusc.2018.12.186.
[42] Z. Wang, Z. Xue, M. Zhang, Y. Wang, X. Xie, P.K. Chu, P. Zhou, Z. Di, X. Wang, Germanium-assisted direct growth of graphene on arbitrary dielectric substrates for heating devices, small 13 (2017), https://doi.org/10.1002/smll.201700929.
[43] X. Chen, B. Wu, Y. Liu, Direct preparation of high quality graphene on dielectric substrates, Chem. Soc. Rev. 45 (2016) 2057–2074, https://doi.org/10.1039/C5CS00542F.
[44] P.W. Sutter, J.-I. Flege, E.A. Sutter, Epitaxial graphene on ruthenium, Nat. Mater. 7 (2008) 406, https://doi.org/10.1038/nmat2166.
[45] A. Reina, X. Jia, J. Ho, D. Nezich, H. Son, V. Bulovic, M.S. Dresselhaus, J. Kong, Large area, few-layer graphene films on arbitrary substrates by chemical vapor deposition, Nano Lett. 9 (2008) 30–35, https://doi.org/10.1021/nl801827v.
[46] A. Reina, S. Thiele, X. Jia, S. Bhaviripudi, M.S. Dresselhaus, J.A. Schaefer, J. Kong, Growth of large-area single-and bi-layer graphene by controlled carbon precipitation on polycrystalline Ni surfaces, Nano Res. 2 (2009) 509–516, https://doi.org/10.1007/s12274-009-9059-y.
[47] J. Lahiri, T. S. Miller, A. J. Ross, L. Adamska, I.I. Oleynik, M. Batzill, Graphene growth and stability at nickel surfaces, New J. Phys. 13 (2011) 025001, , https://doi.org/10.1088/1367-2630/13/2/025001.
[48] Z. Zou, L. Fu, X. Song, Y. Zhang, Z. Liu, Carbide-forming groups IVB-VIB metals: a new territory in the periodic table for CVD growth of graphene, Nano Lett. 14 (2014) 3832–3839, https://doi.org/10.1021/nl500994m.
[49] W. Fang, A.L. Hsu, Y. Song, J. Kong, A review of large-area bilayer graphene synthesis by chemical vapor deposition, Nanoscale 7 (2015) 20335–20351, https://doi.org/10.1039/C5NR04756K.
[50] X.Y. Zhang, L. Wang, J. Xin, B.I. Yakobson, F. Ding, Role of hydrogen in graphene chemical vapor deposition growth on a copper surface, J. Am. Chem. Soc. 136 (2014) 3040–3047, https://doi.org/10.1021/ja405499x.
[51] Y. Li, B. Wu, W. Guo, L. Wang, J. Li, Y. Liu, Tailoring graphene layer-to-layer growth, Nanotechnology 28 (2017) 265101, , https://doi.org/10.1088/1361-6528/aa730b.
[52] P. Yang, J. Prater, W. Liu, J. Glass, R. Davis, The formation of epitaxial hexagonal boron nitride on nickel substrates, J. Electron. Mater. 34 (2005) 1558–1564 (doi:10.1007%2Fs11664-005-0165-7).
[53] T.B. Massalski, Binally Alloy Phase Diagrams, American society for metals, 1986.
[54] R. Abdulrahman, A. Hendry, Solubility of nitrogen in liquid nickel-based alloys, Metall. Mater. Trans. B 32 (2001) 1103–1112 (doi:10.1007%2Fs11663-001-0098-3).
[55] Y. KOJIMA, Y. YAMADA, M. INOUYE, The Solubilities and diffusion coefficients of nitrogen in the liquid Iron-nickel and Iron-cobalt alloys at 1600 °C, Tetsu-to-Hagane 61 (1975) 195–201, https://doi.org/10.2355/tetsutohagane1955.61.2_195.
[56] E. Loginova, N.C. Bartelt, P.J. Feibelman, K.F. McCarty, Evidence for graphene growth by C cluster attachment, New J. Phys. 10 (2008) 093026, , https://doi.org/10.1088/1367-2630/10/9/093026.
[57] J.C. Ganley, F. Thomas, E. Seebauer, R.I. Masel, A priori catalytic activity correlations: the difficult case of hydrogen production from ammonia, Catal. Lett. 96 (2004) 117–122, https://doi.org/10.1023/B:CATL.0000030108.50691.d4.
[58] Z. Xie, S. Ni, M. Song, Effect of Y2O3 doping on FCC to HCP phase transformation in cobalt produced by ball milling and spark plasma sintering, Powder Technol. 324 (2018) 1–4, https://doi.org/10.1016/j.powtec.2017.10.044.
[59] K. Rasim, M. Bobeth, W. Pompe, N. Seriani, A microkinetic model of ammonia decomposition on a Pt overlayer on au (1 1 1), J. Mol. Catal. A Chem. 325 (2010) 15–24, https://doi.org/10.1016/j.molcata.2010.03.021.
[60] B. Wu, D. Geng, Z. Xu, Y. Guo, L. Huang, Y. Xue, J. Chen, G. Yu, Y. Liu, Self-organized graphene crystal patterns, NPG Asia Materials 4 (2012) e36, https://doi.org/10.1038/am.2012.68.
[61] Z. Fan, N. Newman, Kinetic energy distribution of nitrogen ions in an electron cyclotron resonance plasma, J. Vac. Sci. Technol. A 16 (1998) 2132–2139, https://doi.org/10.1116/1.581320.
[62] T. Fu, N. Newman, E. Jones, J. Chan, X. Liu, M. Rubin, N. Cheung, E. Weber, The influence of nitrogen ion energy on the quality of GaN films grown with molecular beam epitaxy, J. Electron. Mater. 24 (1995) 249–255, https://doi.org/10.1007/BF02659683.
[63] Y. Hao, M. Bharathi, L. Wang, Y. Liu, H. Chen, S. Nie, X. Wang, H. Chou, C. Tan, B. Fallahazad, The role of surface oxygen in the growth of large single-crystal graphene on copper, Science (2013) 1243879, , https://doi.org/10.1126/science.1243879.
[64] Y.Y. Stehle, X. Sang, R.R. Unocic, D. Voylov, R.K. Jackson, S. Smirnov, I. Vlassiouk, Anisotropic etching of hexagonal boron nitride and graphene: question of edge terminations, Nano Lett. 17 (2017) 7306–7314, https://doi.org/10.1021/acs.nanolett.7b02841.
[65] N.L. McDougall, J.G. Partridge, R.J. Nicholls, S.P. Russo, D.G. McCulloch, Influence of point defects on the near edge structure of hexagonal boron nitride, Phys. Rev. B 96 (2017) 144106, , https://doi.org/10.1103/PhysRevB.96.144106.
[66] Y. Saito, Statistical Physics of Crystal Growth, World Scientific, 1996.
[67] Z. Zhang, M.G. Lagally, Atomistic processes in the early stages of thin-film growth, Science 276 (1997) 377–383, https://doi.org/10.1126/science.276.5311.377.
[68] R.S. Weatherup, B.C. Bayer, R. Blume, C. Ducati, C. Baehtz, R. Schlogl, S. Hofmann, In situ characterization of alloy catalysts for low-temperature graphene growth, Nano Lett. 11 (2011) 4154–4160, https://doi.org/10.1021/nl202036y.
[69] B.C. Bayer, D.A. Bosworth, F.B. Michaelis, R. Blume, G. Habler, R. Abart, R.S. Weatherup, P.R. Kidambi, J.J. Baumberg, A. Knop-Gericke, In situ observations of phase transitions in metastable nickel (carbide)/carbon nanocomposites, J. Phys. Chem. C 120 (2016) 22571–22584, https://doi.org/10.1021/acs.jpcc.6b01555.
[70] J. Xu, M. Saeys, First principles study of the stability and the formation kinetics of subsurface and bulk carbon on a Ni catalyst, J. Phys. Chem. C 112 (2008) 9679–9685, https://doi.org/10.1021/jp711497q.
[71] X. Liang, B.A. Sperling, I. Calizo, G. Cheng, C.A. Hacker, Q. Zhang, Y. Obeng, K. Yan, H. Peng, Q. Li, Toward clean and crackless transfer of graphene, ACS Nano 5 (2011) 9144–9153, https://doi.org/10.1021/nn203377t.
[72] L.H. Li, J. Cervenka, K. Watanabe, T. Taniguchi, Y. Chen, Strong oxidation resistance of atomically thin boron nitride nanosheets, ACS Nano 8 (2014) 1457–1462, https://doi.org/10.1021/nn500059s.
[73] C. Gong, H.C. Floresca, D. Hinojos, S. McDonnell, X. Qin, Y. Hao, S. Jandhyala, G. Mordi, J. Kim, L. Colombo, Rapid selective etching of PMMA residues from transferred graphene by carbon dioxide, J. Phys. Chem. C 117 (2013) 23000–23008, https://doi.org/10.1021/jp408429v.
[74] R. Arenal, A. Ferrari, S. Reich, L. Wirtz, J.-Y. Mevellec, S. Lefrant, A. Rubio, A. Loiseau, Raman spectroscopy of single-wall boron nitride nanotubes, Nano Lett. 6 (2006) 1812–1816, https://doi.org/10.1021/nl0602544.
[75] J. Deng, G. Chen, X. Song, Characterization of cubic boron nitride thin films deposited by RF sputter, International Journal of Modern Physics B 16 (2002) 4339–4342, https://doi.org/10.1142/S021797920201539X.
[76] P. Mirkarimi, K. McCarty, D. Medlin, Review of advances in cubic boron nitride film synthesis, Materials Science and Engineering: R: Reports 21 (1997) 47–100, https://doi.org/10.1016/S0927-796X(97)00009-0.
[77] H. Sediri, D. Pierucci, M. Hajlaoui, H. Henck, G. Patriarche, Y.J. Dappe, S. Yuan, B. Toury, R. Belkhou, M.G. Silly, Atomically sharp Interface in an h-BN-epitaxial graphene van der Waals Heterostructure, Sci. Rep. 5 (2015) 16465, , https://doi.org/10.1038/srep16465.